PCCP

PAPER

Cite this: *Phys. Chem. Chem. Phys.*, 2019, **21**, 12881

Reactivity and stability of plasma-generated oxygen and nitrogen species in buffered water solution: a computational study†

Pepijn Heirman, Wilma Van Boxem and Annemie Bogaerts *

Received 1st February 2019,
Accepted 25th May 2019

DOI: 10.1039/c9cp00647h

rsc.li/pccp

Plasma-treated liquids have great potential for biomedical applications. However, insight into the underlying mechanisms and the exact chemistry is still scarce. In this study, we present the combination of a 0D chemical kinetics and a 2D fluid dynamics model to investigate the plasma treatment of a buffered water solution with the kINPen® plasma jet. Using this model, we calculated the gas and liquid flow profiles and the transport and chemistry of all species in the gas and the liquid phase. Moreover, we evaluated the stability of the reactive oxygen and nitrogen species after plasma treatment. We found that of all species, only H_2O_2, HNO_2/NO_2^-, and HNO_3/NO_3^- are stable in the buffered solution after plasma treatment. This is because both their production and loss processes in the liquid phase are dependent on short-lived radicals (*e.g.* OH, NO, and NO_2). Apart from some discrepancy in the absolute values of the concentrations, which can be explained by the model, all general trends and observations in our model are in qualitative agreement with experimental data and literature.

Introduction

Cold atmospheric plasma is gaining increasing interest for medical applications, such as wound healing,[1,2] sterilization,[3] blood coagulation,[4] and cancer treatment.[5] However, the underlying mechanisms are not yet fully understood. In general, it is stated that reactive oxygen and nitrogen species (RONS) can affect the signaling pathways in treated cells, inducing several different effects on these cells and the surrounding tissue.[6,7]

Several cold plasma sources have been developed to be specifically used for these medical applications. Among these sources are atmospheric pressure plasma jets (APPJs), dielectric barrier discharges (DBDs), and floating-DBDs. Firstly, the research was mainly focused on direct plasma treatment, where the plasma is directly applied on the tissue or cells to be treated. More recently, a novel approach in cold plasma treatment has gained attention in the research field, *i.e.* the use of plasma-treated liquids (PTLs).[8–10] In this method, a liquid is treated by plasma first, so that the RONS are captured in the liquid, after which the liquid can be injected into the tissue. This way, problems with the standardization of direct plasma treatment and the way of delivery in the body are avoided. Moreover, the plasma reactivity can be stored in a liquid and kept stable for several days,[10] so that plasma treatments can be assured even where no plasma source is available. In the literature, several different liquids have been used to produce PTL, *e.g.* water,[11,12] cell culture media,[13–15] phosphate buffered solutions (PBS),[16–18] and Ringer's lactate solution.[19] In medical applications, mostly buffered solutions are used to avoid the decrease in pH in water caused upon plasma treatment.[11]

Although the interest in the use of PTL for medical applications is clearly increasing,[13,20,21] insight into the fundamental mechanisms of the generation of RONS and the activity of PTL is still lagging.[22] Experiments can provide useful information, but due to the very reactive plasma environment, some open questions cannot be answered experimentally. In this case, computational approaches can be of great value to provide an answer to these open questions. Many efforts have been made to simulate the interaction of a DBD with a liquid layer.[23–27] Babaeva *et al.*[23] computationally investigated the interaction of DBD filaments with a liquid layer in 0D. Also in 0D, Chen *et al.*[24] evaluated the plasma–liquid chemistry for a He/O_2 DBD for the application of treating biofilms and biological tissues. Lietz and Kushner[25] provided more detailed information on a DBD treating liquid covered tissue, and Liu *et al.*[26] gained insight into the propagation of reactive species in the liquid phase and the effect of the gap on the simulated plasma chemistry.

Although the gas phase chemistry for plasma jets is extensively studied,[28–31] only a limited number of studies report the interaction between a plasma jet and a liquid. Previously, we reported a combined experimental and computational study on the treatment of PBS with the kINPen® plasma jet, applying a 0D model to

PLASMANT Research group, Department of Chemistry, University of Antwerp, Universiteitsplein 1, BE-2610 Wilrijk, Antwerp, Belgium.
E-mail: annemie.bogaerts@uantwerpen.be

† Electronic supplementary information (ESI) available. See DOI: 10.1039/c9cp00647h

elucidate the reaction mechanisms for the formation of H_2O_2 and HNO_2 in the liquid.[17] Du *et al.*[32] used a 1D drift diffusion model to investigate the mass transfer process from a plasma jet into the liquid. In addition, a few papers reported 2D simulations of the interaction between a plasma jet and a liquid layer. Lindsay *et al.*[33] investigated the transport of a limited number of reactive species produced by a He plasma jet to liquid water in a 2D model using 13 species and 23 reactions. Lietz and Kushner[34] used a 2D plasma hydrodynamics model to study the consequences of H_2O and O_2 admixtures in the feed gas of a He plasma jet. From the same group, Norberg *et al.*[35] investigated the influence of the pulse repetition frequency on the plasma treatment of a reactive liquid layer. In previous work, we demonstrated the first 2D fluid dynamics model to study the transport and accumulation of plasma-generated species in aqueous solution.[36] Nevertheless, this 2D model still had some limitations. We could only simulate a large liquid volume (135 mL) and were not able to extend the simulation after the plasma treatment. Moreover, to compensate for the fact that we could not simulate the plasma discharge due to long calculation times, we had to implement the species and their concentrations based on literature for a similar, though not exactly the same, condition.

In the current work, we present the first combined 2D–0D model, using a 0D chemical kinetics model and a 2D axisymmetric fluid dynamics model, to study the plasma–liquid interaction of a plasma jet with buffered water solution. We use both models in order to combine their advantages, while avoiding their drawbacks. In a 0D model typically extended chemistry sets can be implemented and calculation times are relatively short. On the other hand, a 2D axisymmetric fluid dynamics model gives insights about the spatial behavior, flow patterns and transport of species. However, these demanding simulations result in very long calculation times, thus limiting the chemistry. We significantly improved our previous 2D model, so that it is able to simulate the plasma treatment of 2 mL liquid with the kINPen® IND plasma jet. The treatment of this volume of 2 mL is based on experiments in the context of cancer treatment, where 2 mL of PBS is typically treated in a 12-well plate. This allows us to directly compare our computational results with experiments. Furthermore, we also apply the 2D model to perform a simulation after plasma treatment, in order to reveal the stability of the RONS in the liquid after treatment. This information is useful because of the increasing interest in the storage of PTLs, and thus the need to understand the stability of RONS in the liquid. With this study, we want to provide deeper insight into the production and reactivity of the reactive species formed in a buffered water solution during plasma jet treatment by the combination of a 0D and a 2D model. Moreover, this is the first computational study that focuses on the stability of the reactive species in a buffered water solution after plasma jet treatment.

Computational setup

Fig. 1 illustrates the simulated system of the 2D model. The model is based on the kINPen® IND plasma jet, used to treat a buffered water solution in a well of a 12-well plate. A flow rate of 3 slm of pure argon and a gap (the distance between the nozzle of the plasma jet and liquid surface) of 30 mm are considered. The liquid surface is not flat, as the gas flow during plasma treatment deforms the surface so that a dimple is formed. The shape of the dimple is based on experimental observations using the same set-up as in the simulations. As a moving mesh would be too demanding in calculation time, the dimple is already present from the start, instead of being formed upon plasma treatment. The edges of the simulated system are considered as open boundaries with ambient air on the outside.

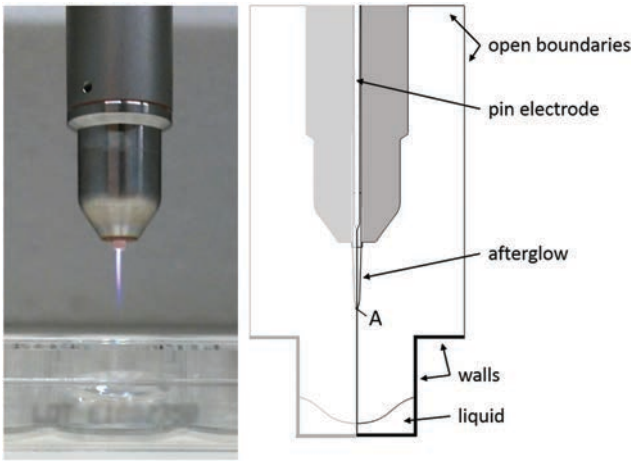

Fig. 1 Left: Picture of the kINPen® plasma jet while treating 2 mL of liquid in a well of a 12-well plate with 3 slm of Ar. Right: Geometry of the simulated system in the 2D model based on the picture on the left. The right part forms the axisymmetric geometry that is considered in the model, while the left part is added to form the full 2D geometry.

We use a combination of a 0D chemical kinetics model and a 2D axisymmetric fluid dynamics model (Fig. 2), to combine the advantages of both types of models and avoid some disadvantages. In a 0D model typically an extended chemistry set can be used, but no dimensional information can be obtained.

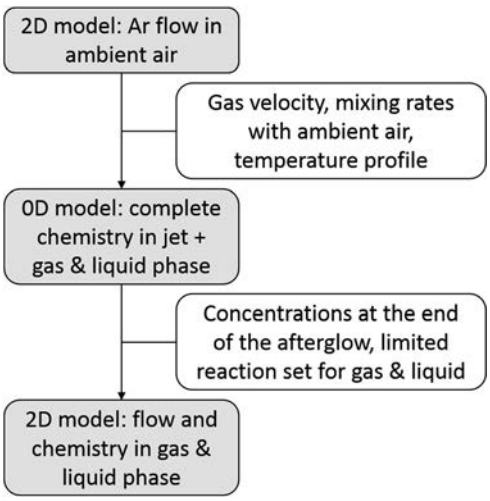

Fig. 2 Overview of the computational flowchart.

The greatest drawback of a 2D model is the very long calculation times, since many parameters are calculated in a 2D mesh. For the conditions under study, a plasma treatment of 10 seconds took 4 months of calculation time on today's fast workstations. As a comparison, for our previous model,[36] it took 2–5 weeks to simulate 30–60 seconds of plasma treatment. The main reason for the longer calculation time in the present setup is that we now consider a smaller liquid volume (2 mL instead of 135 mL) to be able to directly compare with experiments.

Because of these demanding calculations, we use the 0D model to obtain information on the detailed chemistry, to reveal the most important species and reactions, so that the number of reactions included in the 2D model can be limited. In practice, we don't consider the plasma discharge in the 2D model, to reduce the calculation time. Therefore, the densities of the most important reactive species at the end of the visible afterglow (12 mm below the nozzle of the plasma jet, point A in Fig. 1) are used as input for the 2D model, in which the spatial concentrations are calculated. To make sure that both models are fully consistent with each other, we first applied the 2D model to simulate a gas flow of pure argon as the feed gas for the plasma jet, without other species or reactions. This simulation provides the gas flow rate, the temperature profile, and the mixing rate of the argon flow with the surrounding air, to be used as input for the 0D model (see the flowchart in Fig. 2).

The 0D model was already used in previous work.[17,29–31] It is based on solving balance equations for the various species as a function of time, with production and loss rates determined by the chemical reactions. By introducing the velocity profile of the feed gas (taken from the first calculation in 2D, see above), the time can be coupled to the position along the axis, which allows us to obtain information about the species densities as a function of distance, and thus to calculate the species densities at the end of the afterglow. 91 different gas phase species and 43 different liquid phase species are included in this model (see Table 1), which react in 1390 gas phase and 89 liquid phase reactions (Table S1 in the ESI†). Note that H_2O^- is not a stable species in the liquid phase. However, it is included in the model, because it is important in the interface. Indeed, the electrons will ionize the H_2O molecules, forming H_2O^-, which then quickly reacts further (either by charge transfer with OH or O_2, or by dissociation into H atoms and OH^- ions).

In practice, we used the ZDPlasKin code.[37] The gas phase chemistry was extensively validated through experiments,[29,30,38] and also for the liquid phase the concentrations of H_2O_2 and HNO_2 were in good agreement with experiments.[17] More details about the 0D model can be found in the ESI.†

For the 2D model, a 2D axisymmetric fluid dynamics model is developed within Comsol Multiphysics (version 5.3). Four different physical modules are used for both the gas and the liquid phase: turbulent flow to obtain the fluid velocities, heat transfer, transport of diluted species, and chemistry. These modules are set up separately for the gas and the liquid phase, but the two phases are coupled through the gas–liquid interface (see below). More detailed information about the modules and formulas used can be found in the ESI.†

Turbulent flow

A mass flow rate of 3000 sccm (or 3 slm) of argon is used as the input velocity at the inlet of the plasma jet (*i.e.*, top in Fig. 1). Both in the gas and the liquid phase a turbulent flow (k–ε turbulence model, as built in Comsol Multiphysics) is used. This turbulence model is a widely used and well-established model for the description of a turbulent fluid flow. For this model, a Reynolds number of *ca.* 2200 is obtained in the gas phase, which is higher than the typical limit value of 2100 above which a turbulent flow is considered.[39] More detailed information can be found in ref. 40. The velocities are calculated until a steady state is reached using the time-independent Navier–Stokes equations. The gas flow over the liquid surface creates a shear stress on the upper liquid layers. This causes a movement of the liquid in the same direction as the gas flow. The latter is introduced in the simulations by considering the top of the liquid as a sliding boundary with the same velocity as the gas phase at the gas–liquid interface. The steady state velocities in the gas and the liquid phase are used as input values for the transport of heat and species.

Heat transfer

The initial temperature of the gas and the liquid phase is set to 295 K. According to ref. 41 the gas temperature in the kINPen is 327 K. Both the inflowing gas and the inside walls of the plasma jet are thus set to 327 K. All the other walls are considered to be insulating, except for the open boundaries, of which the outside temperature is also kept at 295 K. Through the gas–liquid interface a continuous heat flow is considered, implemented by keeping the gas–liquid boundary at the temperature of the liquid and the gas phase on the side of the gas and the liquid phase, respectively. An additional heat flux is considered over the gas–liquid interface, accounting for the heat loss in the

Table 1 Species included in the 0D model. All species are included in the gas phase, while in the liquid phase only the species in bold are taken into account

Ground state neutrals	Excited state neutrals	Charged species
Ar	$Ar(^4S[^3P_2])$, $Ar(^4S[^3P_1])$, $Ar(^4S[^3P_0])$, $Ar(^4S[^1P_1])$, Ar(4P)	$\mathbf{e^-}$, Ar^+, Ar_2^+, ArH^+
N, N_2	$N(^2D)$, $N(^2P)$, $N_{2,vib(1-4)}$, $N_{2,rot}$, $N_2(A^3\Sigma_u^+)$, $N_2(a'^1\Sigma_u^-)$	N^+, N_2^+, N_3^+, N_4^+
O, O_2, O_3	$O(^1D)$, $O(^1S)$, $O_{2,vib(1-5)}$, $O_{2,rot}$, $\mathbf{O_2(a^1\Delta_g)}$, $O_2(b^1\Sigma_g^+)$	O^+, O_2^+, O_4^+, O^-, $\mathbf{O_2^-}$, O_3^-
NO, NO_2, NO_3, N_2O, N_2O_3, N_2O_4, N_2O_5		NO^+, NO_2^+, N_2O^+, NO^-, $\mathbf{NO_2^-}$, $\mathbf{NO_3^-}$
H, H_2, OH, H_2O, HO_2, H_2O_2	H*, $H_{2,vib}$, $H_{2,rot}$, H_2*, OH(A)	H^+, H_2^+, H_3^+, OH^+, H_2O^+, $\mathbf{H_3O^+}$, H^-, $\mathbf{OH^-}$, $O_2H_2O^-$, $\mathbf{H_2O^-}$, $\mathbf{HO_2^-}$
NH, HNO, HNO_2, HNO_3, HNO_4, **ONOOH**		$NO_2H_2O^-$, $NO_3H_2O^-$, $\mathbf{ONOO^-}$

liquid due to evaporation of water into the gas phase. The value of this evaporation of heat is based on experimental results, where the liquid temperature was measured for different setups.

Transport of species and chemistry

As mentioned before, the plasma treatment of a buffered water solution with an argon plasma jet in ambient air is considered. The initial gas properties are based on ambient air (78.09% N_2, 20.95% O_2, 0.96% H_2O) with a pressure of 1 atm. The liquid is defined as buffered water, with a pH of 7.3, equal to that of PBS (phosphate buffered solution), which is often used in experiments. To keep this pH constant, the concentrations of OH^- and H_3O^+ are kept at 1.995×10^{-7} M and 5.012×10^{-8} M, respectively. This assumption of constant pH was verified experimentally, as we measured the pH before and after the experiments, and we did not observe any change for the conditions under study (*i.e.* treatments up to 5 min). In this study, we do not consider chlorine species (present in PBS) in order to avoid longer calculation times. This assumption is justified because our experiments showed that these species do not really affect the RONS chemistry. Indeed, we measured the H_2O_2 and HNO_2 concentrations (which are the main species) in the plasma-treated solutions for three different orders of magnitude of chlorine concentrations in PBS, and the results were not significantly different (results not shown). In addition, we do not include phosphate ions (also present in PBS) in the model. To the best of our knowledge, no information about the importance of these species in plasma-treated solutions or about reactions with phosphate ions (and their rate coefficients) can be found in the literature. The species included in the model in the gas and the liquid phase are listed in Table 2. Based on the importance of the species in the 0D model and the knowledge of their possible biological effects, these 21 gas phase and 25 liquid phase species are implemented in the model. Some species, like O_2(1D) in the liquid phase and ONOOH in the gas phase, are not included, given the limited knowledge of their chemistry. Since the 2D model does not consider the plasma discharge, no electrons or excited species are included here.

The inlet concentrations (Table S2, ESI†) are taken from the 0D model at the end of the visible afterglow (point A in Fig. 1). In the 2D model, the inlet is defined at the top of the plasma jet in Fig. 1. However, since reactions in the 2D model only take place outside the visible afterglow, the concentrations of the species will still be equal at the end of the visible afterglow, *i.e.* where the reactions start. The transport of the species in both the gas phase and the liquid phase is determined by diffusion and convection. Diffusion is dependent on the diffusion constants of each species (Table S2, ESI†), while convection is governed by the gas and liquid velocity, calculated in the turbulent flow module (see above). The transport over the gas–liquid interface is controlled by Henry's law, for which every species has a temperature-dependent Henry's constant (Table S2, ESI†).

The concentrations of the species in the gas and the liquid phase are not only determined by their transport, but also by their production and loss due to the gas and liquid phase reactions, implemented in the chemistry module. Based on the importance of the reactions in the 0D model, 56 gas-phase reactions (Table S3, ESI†) and 52 liquid-phase reactions (Table S4, ESI†) are included in the 2D model.

Heat transfer and the transfer and chemistry of species are calculated simultaneously in a time-dependent study for a plasma treatment of 10 seconds.

Calculation after plasma treatment

To determine the stability of the liquid species after plasma treatment, we extended our model with another simulation. The inlet concentrations of the species are set to zero and a short time-dependent calculation (0.33 seconds) of the flow, together with the heat transfer, transport of diluted species, and chemistry, is carried out until the flow is faded out. Afterwards, during another 9.67 seconds, the heat transfer, transport of diluted species and chemistry are calculated, so that in total 10 seconds after plasma treatment is calculated. This simulation time may seem quite short in order to reveal the stability of the reactive species in the liquid. However, as will be shown in the results, 10 seconds is long enough to determine the most important findings about the lifetime of the species after plasma treatment. In addition, a longer after-treatment simulation time would unnecessarily extend the calculation time.

Experimental

To validate the model, we measured the concentrations of H_2O_2, HNO_2 and HNO_3 after plasma treatment with the kINPen® IND of PBS in a 12-well plate, under the same conditions as used in the model. The plasma treatment time was 5 minutes.

For the detection of H_2O_2 we applied colorimetry, using the titanium sulphate method.[42] We added NaN_3 to the solutions in order to avoid the destruction of H_2O_2 by NO_2^-.[17] The absorbance measurements of the formed peroxytitanium(IV) complex were done with a ThermoFischer Genesys™ 6 spectrophotometer at a wavelength of 400 nm. The quartz cuvettes have a path length of 1 cm, an internal width of 2 mm, and a volume of 700 μL. For the measurements we added 50 μL N_3^- solution (80 mM NaN_3 in PBS), 200 μL sample and 50 μL

Table 2 Gas and liquid phase species included in the 2D model

	Gas phase	Liquid phase
Molecules	O_2, O_3, H_2, HO_2, H_2O_2, H_2O, N_2, HNO, HNO_2, HNO_3, N_2O, Ar	O_2, O_3, H_2, HO_2, H_2O_2, N_2, HNO, HNO_2, HNO_2, N_2O, ONOOH
Radicals	O, H, OH, N, NH, NO, NO_2, NO_3	O, H, OH, N, NH, NO, NO_2, NO_3
Excited species	O_2(1D)	
Ions		O_2^-, OH^-, H_3O^+, NO_2^-, NO_3^-, $ONOO^-$

Ti(IV)-solution (0.1 M $K_2TiO(C_2O_4)_2{\cdot}2H_2O$ and 5 M H_2SO_4 in Milli-Q water) to the cuvette and we shook thoroughly.

To measure the NO_2^- and NO_3^- concentrations, we used a nitrate/nitrite colorimetric assay kit (Cayman Chemical, 780001) according to the provided protocol. The detection of NO_2^- was done with Griess reagents. For NO_3^- a nitrate reductase enzyme and cofactor were used to reduce NO_3^- to NO_2^-, and subsequently it was detected with Griess reagents. It must be realized that this detection method is not very accurate, as it might yield a systematic underestimation due to effectivity loss in plasma-treated solutions. However, we had no access to more accurate methods, like ion chromatography. Nevertheless, this limitation must be taken into account when comparing our calculation results with the experimental data. The absorbance was measured in a 96-well plate with a BIO-RAD iMark™ microplate reader at 540 nm.

Results and discussion

Flow profile in the gas and the liquid phase

The calculated steady state flow profile is shown in Fig. 3. The inlet flow rate of 3 slm argon results in a maximum gas velocity of 57 m s^{-1} inside the plasma jet. The maximum gas velocity outside the plasma jet is 34 m s^{-1}. When the gas flow reaches the liquid surface, it flows towards the edge of the well, causing a shear stress on the liquid surface. Hitting the wall of the well, the gas flow results in a vortex within the well so that the gas flows back towards the afterglow.

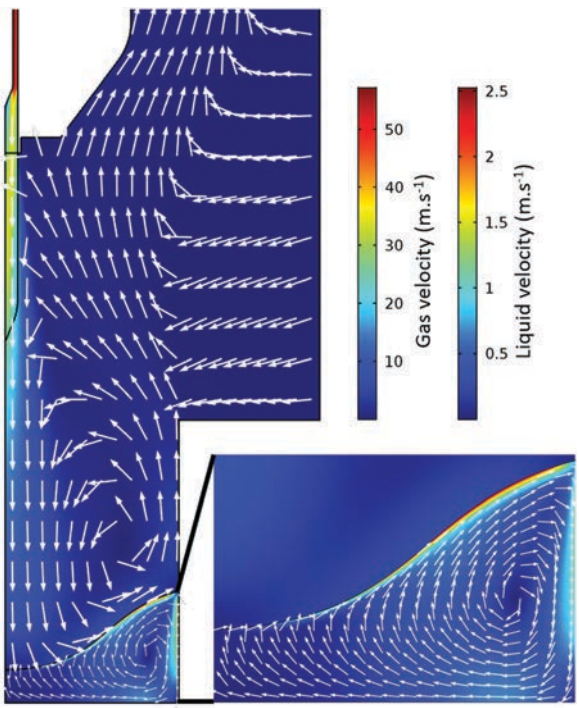

Fig. 3 Visualization of the steady state gas and liquid flow, and details of the liquid flow, calculated in the model for an inlet flow rate of 3 slm of Ar. The magnitude of the velocity is given by the colour range, while the arrows show the direction of the flow. The size of the arrows does not correlate to the magnitude. The maximum velocity in the area in the upper right, where the gas flows inwards from the open boundary, is only 0.05 m s^{-1}. The upwards gas stream next to the plasma jet housing is 0.7 m s^{-1} next to the nozzle, and at maximum 0.3 m s^{-1} at the top of the calculated area. In the bulk of the gas, around the vortex, the gas velocity varies between 1 and 5 m s^{-1}, while the bulk liquid velocity, around the vortex, is about 0.5 m s^{-1}.

Because of the shear stress on the liquid surface, the upper layer of the liquid will start moving in the same direction as the gas, but with a lower velocity. The maximum velocity in the liquid is reached near the edge of the well (*i.e.* 2.5 m s^{-1}). The liquid movement makes another vortex in the liquid phase, occupying the whole well, so that in the middle of the well the liquid goes back up, in the direction of the surface. At first sight this may seem contradictory with our previous findings[36] where 2 vortices were formed in the liquid phase. However, in this study a much lower liquid volume is used, so it is logical that only 1 vortex occupies the whole vessel. Van Rens *et al.*[43] also studied the induced liquid phase flow by the kINPen®. They observed a different flow pattern in the treated liquid. However, their plasma treatment conditions were also very different. In their experiments, the plasma plume was in contact with the liquid surface. As they also observed, the presence of a net electrical field and charging of the water surface due to the ion flux can cause a different liquid flow pattern. In our experiments, the gap between the plasma jet and the liquid surface is larger (30 mm *vs.* 12 mm), so this can explain the different liquid flow pattern for our setup.

The gas and liquid velocity fields are used as input for (1) the 0D model (see Computational setup), and (2) the 2D simulations of heat transfer and chemical transport.

Gas phase concentrations

Fig. 4 shows the gas phase densities of the reactive oxygen and nitrogen species (upper and lower panels, respectively) as a function of distance from the end of the afterglow (point A in Fig. 1) after 10 seconds of plasma treatment. On the left side, the densities calculated in the 0D model are shown, while on the right side, the corresponding densities calculated in the 2D model are plotted. It is clear that the gas phase densities calculated with the 2D model are comparable with those from the 0D model. This means that although the chemistry set is reduced from 91 gas phase and 43 liquid phase species (Table 1) and from 1390 gas phase and 89 liquid phase reactions (in the 0D model) to 21 gas phase and 25 liquid phase species (Table 2) and to 56 gas phase and 52 liquid phase reactions (Tables S3 and S4, ESI†) (in the 2D model), the chemistry for the neutral long-lived species is correctly implemented in the 2D model.

Overall, these gas phase density profiles are also in good qualitative agreement with the previous computational work of Van Gaens and co-workers[30,44] where a similar Ar plasma jet was used, and for which several plasma species were validated with experiments. One remarkable difference in our results is that the NO gas phase density increases in the afterglow, while Van Gaens *et al.* predict a drop in its density in the afterglow. This is due to the different approach between the calculations of Van Gaens *et al.* and the present model (both 0D and 2D).

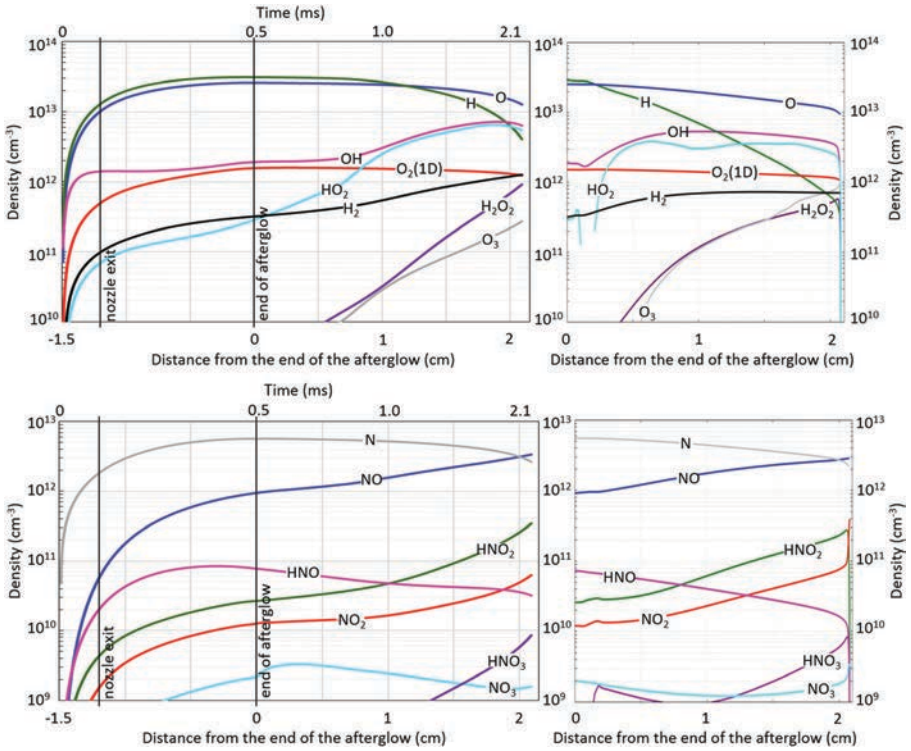

Fig. 4 Comparison of the gas phase densities of the ROS (upper panels) and RNS (lower panels) underneath the nozzle of the plasma jet, calculated by the 0D (left) and the 2D (right) model. For the 0D model, the densities are calculated as a function of time (upper x-axis), which can be converted to distance (lower x-axis) based on the gas velocity. The calculation starts at the end of the pin electrode and ends at the liquid surface. The afterglow ends at a distance of 1.5 cm from the pin electrode of the plasma jet. For the 2D model, the densities are calculated from the end of the afterglow until the liquid surface.

Indeed, Van Gaens *et al.* considered a free plasma jet, meaning that outside the plasma jet there was just air, with no specific obstacles in the effluent. In our case, the model is based on the experimental setup shown in Fig. 1, where a well is put underneath the plasma jet. This results in a very different mixing with the ambient air than in the case of a free jet. Indeed, we found that within half a second of plasma treatment, almost all ambient air is blown away out of the well (see Fig. 5), and because of the small dimensions and high velocities, the ambient air cannot reach the plasma jet afterglow anymore during treatment. The Ar density at the side of the jet outlet is between 1×10^{19} and 2×10^{19} cm^{-3}. This much lower mixing with the ambient air in our model results in an overall lower density of the NO radical. Because of this, the loss reactions are less important and the NO density is increasing in the afterglow.

It should be noted that the gas phase densities of some species (O_3 and NO_2) as calculated by our model are one or two orders of magnitude lower than what was found in previous work. For example, the O_3 concentrations in the far field were one to two orders of magnitude higher in Schmidt-Bleker *et al.*[41] and

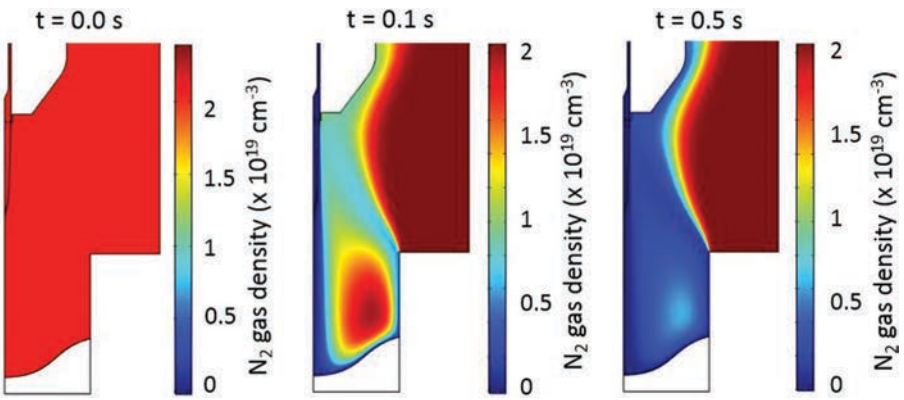

Fig. 5 2D plots of the N_2 density in the gas phase at different time points. At t = 0 s, it is clear that the whole system is filled with ambient air. Already after 0.1 s a large fraction of the N_2 gas is blown away out of the well, and after 0.5 s almost no N_2 is present between the plasma jet and the liquid surface inside the well. O_2 behaves exactly the same as N_2 (results not shown).

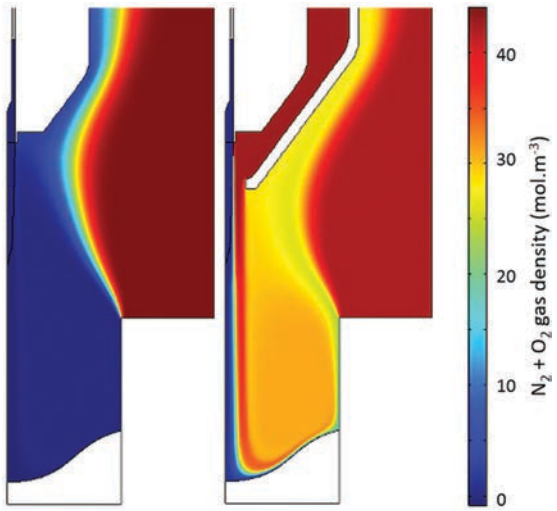

Fig. 6 2D-plots for the density of air (N_2 + O_2) after a plasma treatment of 10 seconds for the system without a gas shield (left) and for the system with a gas shield (right).

Hansen *et al.*[45] than in our results. These two papers, however, use a shielding gas around the effluent of the plasma jet. To verify whether our reaction kinetics model is correct, we performed simulations to mimic the conditions of Schmidt-Bleker *et al.*[41] and Hansen *et al.*[45] As in both papers a shielding gas device was used, we also added this in our model (see details in the ESI;† Section S3). In Fig. 6 we plot the air density (*i.e.* N_2 + O_2) after 10 seconds of plasma treatment for our original model (left) and the model with shielding gas (right). It is clear that after 10 seconds still a lot of air is present inside the well in the case of using a shielding gas. Since the production of O_3 largely depends on the presence of O_2, this explains why the O_3 concentration in our model without shielding gas is significantly lower than when a shielding gas is used, as in Schmidt-Bleker *et al.*[41] and Hansen *et al.*[45] (see detailed discussion in the ESI;† Section S3). However, the use of a shielding gas cannot explain the lower NO_2 concentration in our model. As explained in detail in the ESI† (Section S3), this might be due to the presence of the liquid surface (more specifically, the different gap between the plasma jet and the liquid surface) or the impurities implemented in the feed gas.

General behaviour of species

In Fig. 7 we plot the gas phase density and liquid phase concentration of H_2O_2, HNO_2 and HNO_3 after 10 seconds of plasma treatment. For HNO_2 and HNO_3 the sum of the acid HNO_x and the negative ion NO_x^- is taken as the liquid phase concentration. First of all, it is clear that the density profiles in the gas phase and the liquid concentration profiles of the species follow the velocity field shown in Fig. 3. Indeed, because of the high velocities, the convection of the species is more important than diffusion. The different behaviour of these species in the gas phase is clearly visible. The H_2O_2 density is the highest underneath the plasma jet, just above the liquid surface. Its density drops to half its value towards the edge of the wall and in the bulk gas. HNO_2 is only formed to a small extent underneath the plasma jet just above the surface, but its density is the highest towards the edge of the well and in the bulk gas. The HNO_3 density, on the other hand, is not rising at all underneath the plasma jet. Its concentration is the highest in the bulk gas, further from the liquid surface than the HNO_2 density. It is clear that the densities of HNO_2 and HNO_3 accumulate in the vortex in the gas phase. Indeed, at the edge in the well, the species are redirected towards the effluent of the plasma jet. Since the upwards velocity is quite low, the species accumulate inside this vortex. Also H_2O_2 accumulates inside this vortex. However, this is not clearly visible, because the density of H_2O_2 just above the liquid surface in the middle of the well is a factor 2–2.5 higher than inside the vortex (which is not the case for HNO_2 and HNO_3, which exhibit the highest densities inside the vortex).

When looking at the transport of the species from the gas into the liquid phase, and as a consequence the behaviour of their profiles just above and below the liquid surface, it is important to account for the Henry's constants. H_2O_2, HNO_2, and HNO_3 all have a high Henry's constant (*i.e.* greater than 1), which means their equilibrium is towards the liquid phase. This is seen in the difference between the gas phase density profile just above the liquid surface, and the liquid phase concentration profile just below the liquid surface (see the close-ups in Fig. 7). The gas phase density of the three species is very low just above the liquid surface, because the species are transported towards the liquid, and as a consequence removed from the gas phase in a few nm above the liquid surface. In the upper layer of the liquid the opposite trend is observed. The liquid concentration is the highest in the first few nm below the liquid surface, because of the import from the gas phase, after which the species follow the liquid flow and are redistributed over the liquid volume. Since the HNO_2 and HNO_3 densities in the gas phase are the highest towards the edge of the well, these species will be mostly imported into the liquid phase at this position, while H_2O_2 will be transported into the liquid mainly in the center of the well (underneath the plasma jet). Note that the highest concentration of H_2O_2 is calculated to be ten times greater than that of HNO_2, which is in its turn ten times greater than that of HNO_3 (*cf.* different values on the color scales). This does not tell us anything about the total liquid concentration, since the latter is also affected by the redistribution over the liquid volume and by the liquid phase reactions of the species (see below). In the liquid the concentrations of the species follow the liquid velocity profile shown in Fig. 3, which results in a depression of the concentrations in the center of the liquid vortex. This is because the species do not get into the vortex, but are redirected towards the center of the well along the edge and bottom of the well.

In Fig. 8 we plot the gas phase densities and liquid concentrations for some other important RONS, *i.e.*, O_3, HO_2, NO, OH, and NO_2. O_3 exhibits a similar behaviour to HNO_2 (see Fig. 7). HO_2 is only highly present just outside the visible afterglow, and does not accumulate into the liquid as much as H_2O_2, HNO_2, HNO_3 and O_3. The concentration of NO is high both below the plasma jet and in the bulk gas. OH is only present on the axis below the plasma jet, and NO_2 is also accumulating into the gas phase vortex. For OH,

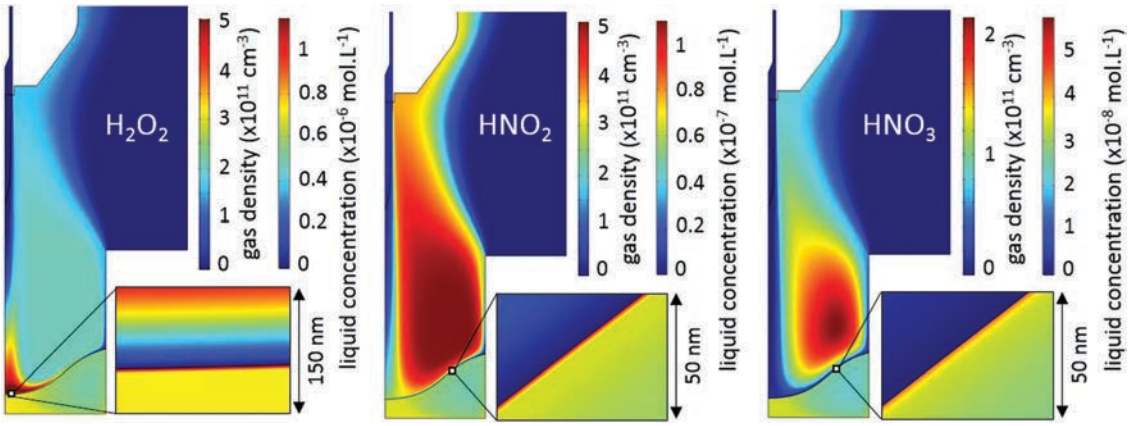

Fig. 7 2D plots of the gas phase densities and liquid phase concentrations of selected species after 10 seconds of plasma treatment. A zoom of the gas–liquid interface is shown in the frame. For H_2O_2 this detail is shown for a position underneath the plasma jet, while for HNO_2 and HNO_3 it is taken for a position more towards the edge of the well, explaining the difference in slope of the liquid surface. The gas phase densities are plotted in 10^{11} cm^{-3}, while the liquid phase concentrations are plotted in 10^{-6}, 10^{-7}, and 10^{-8} mol L^{-1} for H_2O_2, HNO_2, and HNO_3, respectively.

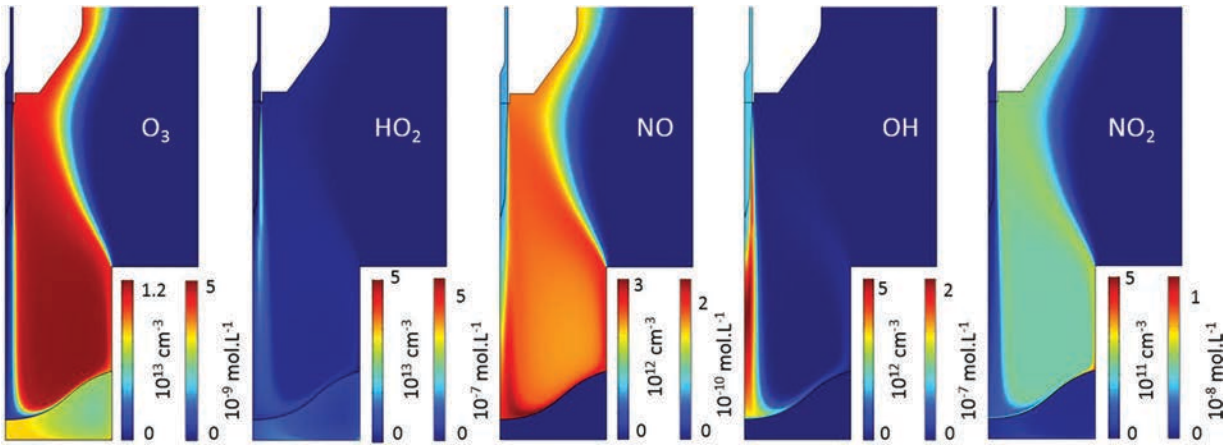

Fig. 8 2D plots of the gas phase densities and liquid phase concentrations of selected species after 10 seconds of plasma treatment. The left colour scale shows the gas phase density, while the right colour scale shows the liquid concentration. For the short-lived species NO, OH, and NO_2 no clear concentration profile in the liquid phase is visible, because these species are only present in the first few nm below the gas–liquid interface.

NO, and NO_2 the liquid phase profile is not clearly visible, since their concentrations are only significant in the first few nm below the gas–liquid interface, after which they drop to almost zero. They are not able to accumulate into the bulk liquid.

It is worth mentioning that ONOOH is not pictured here, since it is only present in the liquid phase (see below). The behaviour of O, N, HNO, O_2(1D), NH and H is similar to that of OH, with the only difference that NH and H are not able to reach the liquid surface. The gas phase profile of N_2O looks similar to that of HNO_2 and O_3, and NO_3 in the gas phase behaves the same as HO_2, while H_2 in the gas phase behaves the same as NO. In the liquid phase these species behave the same as the short-lived species presented in Fig. 8 (NO, OH, NO_2, and HO_2).

Total liquid concentration of the long-lived species

Of all liquid phase species, only H_2O_2, HNO_2, HNO_3, HO_2, O_3, and ONOOH are able to accumulate (to some extent) in the liquid (*cf.* Fig. 7 and 8) and are named as long-lived species in the liquid. The other species are too short-lived and are only important in the first few nm below the liquid surface, after which they are completely lost by chemical reactions. For the long-lived species in the liquid, the total liquid concentration can be evaluated through a volume integration over the total liquid volume (*i.e.* 2 mL). The concentration of these species as a function of time is shown in Fig. 9, not only during but also after plasma treatment. Indeed, the plasma treatment takes 10 seconds, after which the plasma is turned off, and another 10 seconds after plasma treatment is simulated. During plasma treatment (*i.e.* time = 0–10 s), three different patterns of concentration change with time can be seen. The concentrations of H_2O_2, HNO_2, and HNO_3 increase linearly over time. For H_2O_2 and HNO_2, this is in agreement with our previous experimental results[17] (HNO_3 was not measured in that work). HO_2, on the other hand, increases very quickly in the first couple of milliseconds, after which it reaches a steady state, which is retained during the total plasma treatment. Finally, the concentrations of

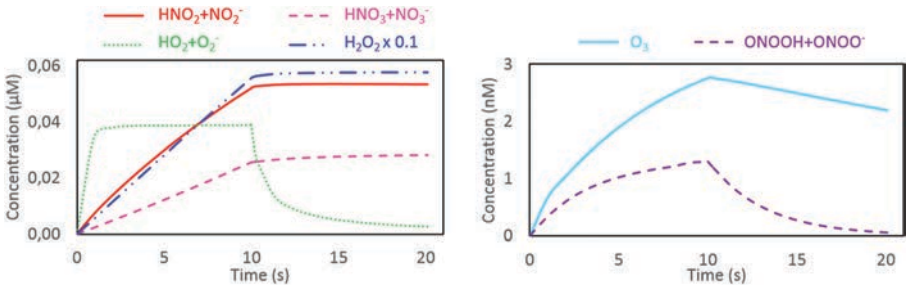

Fig. 9 Total liquid concentrations (calculated by volume integration over the total liquid volume) of the accumulating species as a function of time, during and after plasma treatment. For clarity, the H_2O_2 concentration is shown a factor of 10 lower than its actual concentration. The concentrations of $HNO_2 + NO_2^-$, $HNO_3 + NO_3^-$, $HO_2 + O_2^-$, and H_2O_2 are given in μM (left), while the concentrations of O_3 and ONOOH + $ONOO^-$ are given in nM. During the first 10 seconds the plasma is "on", after which the plasma is switched off, so that the stability of the species in the liquid after plasma treatment can be revealed.

O_3 and ONOOH keep on increasing over time, but the rise clearly flattens as a function of treatment time.

After plasma treatment (time = 10–20 s), it is clear that H_2O_2, HNO_2 and HNO_3 are the only stable species in the liquid. Their concentrations remain constant in the first 10 seconds after plasma treatment. In principle, these species can be lost, but the corresponding reactions are much slower than the radical mechanisms. This is also in agreement with our previous results.[17] Indeed, the H_2O_2 and HNO_2 concentrations did not change in the plasma-treated liquid for up to 2 hours after plasma treatment (HNO_3 was not measured in that work). The concentrations of HO_2 and ONOOH decrease rather quickly after plasma treatment, and after 10 seconds no significant amount of these species is still present. Finally, the O_3 concentration decreases linearly after plasma treatment. 10 seconds after plasma treatment, its concentration has dropped to 80% of its value at the end of the plasma treatment. This linear decrease is due to the transport of O_3 back to the gas phase. Indeed, the Henry constant of O_3 is low (*i.e.* lower than 1), which means that its equilibrium is pointed towards the gas phase. Because the O_3 density above the liquid surface disappears after plasma treatment (because of no supply from the plasma jet), the O_3 concentration in the liquid starts to evaporate. This evaporation will continue until all the O_3 is lost from the liquid phase. According to our simulations, this will last approximately 50 seconds (extrapolation of the O_3 concentration after plasma treatment). For comparison, the lifetime of the short-lived species, like OH, NO, and NO_2, is on the order of a couple of milliseconds (*e.g.* after 5 ms the concentration of OH at the interface has dropped by one order of magnitude, and after 8 ms already by two orders of magnitude).

Validation of the model with experiments

To validate our model, we have also measured the concentrations of H_2O_2, HNO_2, and HNO_3 for the same setup as used in the model, but with an extended treatment time of 5 min, because for a shorter treatment time the concentrations would be too low for detection. Since the concentrations of H_2O_2, HNO_2 and HNO_3 increase linearly over time in the model during plasma treatment, we extrapolated the results of 10 seconds of treatment to 5 minutes of treatment, assuming that the concentrations indeed keep on increasing linearly up to 5 min. Indeed, in our previous experiments, we found that the concentrations of H_2O_2 and HNO_2 increase linearly up to 9 min,[17] and this is probably also true for HNO_3. The experimentally measured concentrations are 186 ± 5, 57 ± 6, and 56 ± 11 μM for H_2O_2, HNO_2, and HNO_3 respectively (keeping in mind however the limitations of the nitrate reductase enzyme, as explained above), while the extrapolated simulated concentrations are 17, 1.6, and 0.77 μM, hence a factor of 11, 37, and 73 too low for H_2O_2, HNO_2, and HNO_3, respectively. Obviously, our model does not provide a good agreement yet with experiments. Thus, we should not focus too much on the absolute values.

Nevertheless, we believe that we can explain the discrepancy caused in the model, and thus how this could be improved in the future. Indeed, in the 2D model a static gas–liquid interface is considered. The only movement at the interface is caused by the shear stress of the gas on the liquid surface. In experiments, however, the liquid surface is moving very turbulently, according to the high gas flow rate and the small liquid vessel. Because transport of the gas phase species into the liquid phase is calculated in the model with Henry's law, which is based on an equilibrium between the gas and the liquid phase, we believe that the transport into the liquid is underestimated in the model. Indeed, in the experiments, the top layer of the liquid will be more often replaced by 'fresh' liquid with a lower concentration of species, so that additional species will be transported into the liquid. This equilibrium between the gas and liquid phase is determined by the Henry's constant of each species. For the three experimentally measured species, the Henry's constant is the highest for HNO_3, followed by H_2O_2, while HNO_2 has the lowest Henry's constant, albeit still pointing towards the liquid phase. Based on the above explanation, if the transport into the liquid is underestimated, the discrepancy of the concentration of species with the highest Henry's constant should be the highest. This is indeed true for HNO_3, but HNO_2 and H_2O_2 act the other way around, since HNO_2 has the lowest Henry's constant but it shows a larger deviation from the experimental concentration than H_2O_2.

However, a static interface does not only affect the transport into the liquid phase, but also the liquid chemistry in the interface region. As will be discussed below, H_2O_2 and HNO_3

are mainly produced in the interface region and their production depends on reactions of radicals, like OH and NO_2. These short-lived species will all be gone in the interface region anyway (*i.e.* because of their short lifetime), so the static interface does not elongate their presence in the interface region. This way, the static interface does not significantly affect the production of H_2O_2 and HNO_3 by chemical reactions. However, since HNO_2 is lost in the interface region due to chemical reactions (see below), the static interface will affect its concentration. Indeed, the static interface causes HNO_2 to stay longer in the interface region than it would in experiments, leading to an overestimation of its loss in the liquid. This explains why HNO_2 and H_2O_2 act the other way around than what is expected based on their Henry's constants. In summary, assuming a static interface in the model will underestimate the liquid concentrations, due to lower mixing of the liquid than in experiments. Up till now, however, simulating a moving liquid surface was not yet feasible, due to very long calculation times. Indeed, the current simulations, with a static interface and for a plasma treatment time of 10 seconds, already took 4 months. However, in future work we will further improve our model and try to make it faster. Therefore, we believe that we will be able in the future to solve this discrepancy of our simulations with experiments. Nevertheless, despite the fact that the calculated liquid species concentrations are not yet in quantitative agreement with the experiments, the model is already very useful to study the chemistry and stability of species in the liquid. A moving interface would only result in different relative amounts of the reactive species, which will not change the overall liquid processes significantly. Thus, apart from the exact values of the concentrations, the general trends can already be determined.

To verify our hypothesis on the effect of the turbulent movement of the liquid interface, we performed additional simulations (see the ESI,† Section S4). More specifically, by comparing our calculation results with Winter *et al.*[46] where H_2O_2-containing argon gas was used without plasma ignition, we can conclude that the transport of species (H_2O_2 in this case) from the gas into the liquid phase is indeed underestimated in our model, and this cannot be attributed to the chemistry (which is absent in this case), but it is most probably due to the turbulent movement of the liquid interface. Hence, we believe that the turbulent movement of the liquid interface should be accounted for. The underestimation of the liquid concentration of H_2O_2 is, however, less pronounced than in our plasma model when compared with our experiments. This could be attributed to the very different geometry used in Winter *et al.*,[46] *i.e.*, a large Petri dish, where the turbulent movement of the liquid surface might not be as prominent as in a small well of our well plate. However, the underestimated liquid concentrations might also be due to a combination of both the static liquid surface and an underestimation of gas phase densities.

Detailed liquid chemistry

The main production and loss reactions for the long-lived species in the liquid during plasma treatment are listed in Table 3. After plasma treatment, the chemistry does not change much, except for the fact that the import from the gas phase stops, and thus also some of the reactions. The most important liquid phase chemistry is also schematically illustrated in Fig. 10.

H_2O_2, HNO_2, and HNO_3. H_2O_2, HNO_2 and HNO_3 have high Henry's constants and thus they are continuously transported from the gas phase into the liquid during plasma treatment. On top of the accumulation of H_2O_2 in the liquid due to transport from the gas phase, there is also a net production of H_2O_2 in the liquid phase. The dominant production of H_2O_2 is caused by the recombination of two OH radicals (reaction (R6)), which occurs only in the first few nm underneath the gas–liquid

Table 3 Most important production and loss reactions for the long-lived species in the liquid (analyzed during plasma treatment) and their contribution to the total production or loss of that species. The numbers indicate the % of contribution for the total liquid chemistry, taken as the average over the total volume. Some of the most important reactions occur only in the interface, which is where most of the chemistry happens, but since the interface region only occupies a small part of the total volume, the % of contribution for the total liquid is almost zero for these interface reactions. These reactions are thus designated with 'IF' (interface) instead of their very low % of contribution. A reaction with a star (*) behind it is the only reaction for the production or loss of that species implemented in the 2D model. The reaction numbers correspond to Table S4 (ESI). Reactions between 2 species resulting in 1 species are possible because of the omnipresence of H_2O molecules in the liquid (conservation of momentum and energy)

Species	Main production reactions	%	Main loss reactions	%
H_2O_2	(6) $2OH \rightarrow H_2O_2$	IF	(9) $H_2O_2 + OH \rightarrow HO_2 + H_2O$	IF
			(14) $H_2O_2 + H \rightarrow OH + H_2O$	100
HNO_2	(33) $NO + OH \rightarrow HNO_2$	IF	(24) $NO_2^- + OH \rightarrow NO_2 + OH^-$	IF
	(27) $2NO_2 + 2H_2O \rightarrow HNO_2 + NO_3^- + H_3O^+$	65	(48) $NO_2^- + N_2O \rightarrow NO_3^- + N_2$	80
	(28) $2NO_2 + 3H_2O \rightarrow NO_2^- + NO_3^- + 2H_3O^+$	25	(25) $NO_2^- + H \rightarrow NO + OH^-$	15
HNO_3	(34) $NO_2 + OH \rightarrow HNO_3$	IF	(35) $HNO_3 + OH \rightarrow NO_3 + H_2O$ (*)	
	(27) $2NO_2 + 2H_2O \rightarrow NO_3^- + HNO_2 + H_3O^+$	65		
	(28) $2NO_2 + 3H_2O \rightarrow NO_3^- + NO_2^- + 2H_3O^+$	25		
ONOOH	(39) $NO_2 + OH \rightarrow ONOOH$	IF	(41) $ONOOH + H_2O \rightarrow NO_3^- + H_3O^+$	IF65–30
	(38) $NO + HO_2 \rightarrow ONOOH$	100	(42) $ONOOH + H_2O \rightarrow NO_2 + OH + H_2O$	IF30–65
HO_2	(9) $H_2O_2 + OH \rightarrow HO_2 + H_2O$	IF	(10) $O_2^- + OH \rightarrow O_2 + OH^-$	IF
O_3	(16) $O_2 + O \rightarrow O_3$ (*)		(37) $O_3 + NO_2^- \rightarrow NO_3^- + O_2$	85
			(45) $O_3 + HNO \rightarrow HNO_2 + O_2$	15

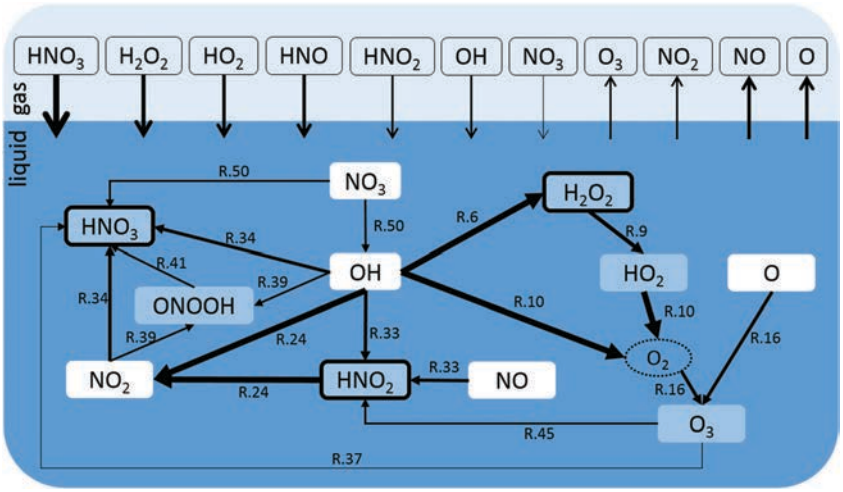

Fig. 10 Schematic overview of the transport of species from the gas to the liquid phase and of the most important liquid chemistry. The down- or upward arrows between the gas and the liquid phase illustrate the transport due to Henry's law. The thickness of the arrows indicates the relative values of the Henry's constants, while the direction of the arrows shows the equilibrium of the species towards the gas or liquid phase. The reaction numbers mentioned on the arrows between the species correspond to the reaction numbers in Tables 3 and 4, and in Table S4 (ESI†). For the importance of these reactions, we refer to Tables 3 and 4, where we have listed their relative contributions (in %) to the overall production or loss of the species. The thickness of the reaction arrows is a measure of the rate of that reaction. Species in a white box are the short-lived species that completely react away just below the gas–liquid interface. Species in a blue box are able to accumulate in the bulk liquid, but only those with a thick black frame are stable in the liquid after plasma treatment. O_2 is only pictured to shown the transition of HO_2 into O_3 over O_2, and is not analysed as a separate species.

interface and also mainly in the center of the well (in the depression of the dimple), because further and deeper into the liquid, there are virtually no OH radicals left. In the same region the loss of H_2O_2 is also mainly caused by OH radicals (R9), while deeper in the bulk liquid the loss of H_2O_2 is caused by reaction with H radicals (R14). It must be noted that the greatest part of the liquid chemistry happens just beneath the gas–liquid interface and that the reaction rates in the bulk liquid are at least three orders of magnitude lower than in the first few nm below the interface. For H_2O_2 the rates of the loss processes are much lower than the production rates (*e.g.* in the interface the rate of the loss reaction (R9) is a factor 50 lower than that of the production reaction (R6)), causing a continuous increase of the H_2O_2 concentration in the liquid phase (see Fig. 9).

HNO_2 and HNO_3 in water partially split into H_3O^+ and NO_2^- or NO_3^- ions, respectively, according to their pK_a values. They can react both in their neutral and ionic form. To evaluate the most important reactions of these species, these neutral and ionic forms are taken together in the analysis. The acid–base reaction is not accounted for in the production or loss terms. The production of HNO_2 is due to the reactions of the short-lived species OH and NO in the interface region (R33), and of NO_2 with H_2O in the bulk liquid ((R27) and (R28)). It is lost mostly in its ionic form in the first 3 nm depth below the gas–liquid interface and in the center of the well, due to reaction with OH radicals (R24). Further in the bulk liquid, the reactions with N_2O and H ((R48) and (R25)) become more important, but again the greatest part of the chemistry happens in the first few nm below the gas–liquid interface. Note that the loss of NO_2^- upon reaction with OH radicals (R24) is two orders of magnitude faster than the production reaction (R33), so HNO_2 exhibits a net loss in the liquid phase due to chemical reactions. Still, its concentration linearly increases, which is due to the constant supply from the gas phase.

For HNO_3, on the other hand, our model predicts a net production in the liquid phase due to chemical reactions. Just below the interface in the first 2 nm depth, this is due to the reaction of OH with NO_2 (R34). Below that, in the next 2 nm, the production rate is still very high and is due to reactions involving NO_2 and H_2O ((R27) and (R28)). Again, the production is the highest in the center of the well, while in the bulk liquid the reaction rates are three orders of magnitude lower than at the interface. The reaction with OH (R35) is the only loss reaction for HNO_3 included in the model. Its rate is a factor 150 lower than that of the main production reaction between NO_2 and OH (R34), explaining the net production of HNO_3 in the liquid phase. Although HNO_3 has a higher Henry's constant than HNO_2 and is net produced by chemical reactions, while HNO_2 is lost in the liquid, the total concentration of HNO_3 is lower than that of HNO_2. This is due to the much lower gas phase density of HNO_3 just above the liquid surface (see Fig. 7), so that less HNO_3 is transported into the liquid phase than HNO_2.

In summary, the liquid chemistry for these three most important species is mainly driven by reactions of short-lived species, like OH and NO_2. For H_2O_2 and HNO_3 there is net production by chemical reactions, while for HNO_2 the loss reactions are faster than the production reactions. It is not surprising that the only significant changes in liquid concentrations are happening in the first few nm below the gas–liquid interface, where indeed these short-lived species are still present before being completely lost by reactions. Because both the production and loss reactions of H_2O_2, HNO_2 and HNO_3 are only based on these very short-lived radicals (OH, NO, and NO_2), which will be completely gone immediately

after the supply of the plasma jet is switched off, H_2O_2, HNO_2 and HNO_3 are not being formed or lost anymore in the liquid after plasma treatment (at least not on the short time scales of relevance here). In addition, because of their high Henry's constants, they will not (significantly) evaporate into the gas phase. Hence, this explains why their concentrations remain constant after plasma treatment (see Fig. 9).

ONOOH, HO_2, and O_3. A similar analysis can be performed for the other three long-lived species: ONOOH, HO_2, and O_3. Just like HNO_2 and HNO_3, ONOOH and HO_2 also partially split in water into H_3O^+ and $ONOO^-$ or O_2^- ions, respectively. To evaluate the most important chemistry, these neutral and ionic forms are again taken together in the analysis. The acid–base reaction is not accounted for in the production or loss terms.

ONOOH is not present in the gas phase in our model, because of a lack of information about its gas phase chemistry. Thus, no ONOOH is transported into the liquid and its concentration only depends on the liquid chemistry. There are a few studies on how peroxynitrite can be formed in the liquid (*i.e.*, in acidic conditions from H_2O_2 and NO_2^-,[47] as well as from reactions between OH and NO_2, and from O_2^- and NO[48,49]). The formation of ONOOH in the gas phase was – to our knowledge – never reported, however, it can be assumed that the reaction between OH and NO_2 radicals also takes place in the gas phase, leading to gaseous ONOOH. By only considering ONOOH in the liquid phase in the model, its total liquid concentration might be underestimated. However, the general behavior of ONOOH will still be valid in the case of additional transport from the gas into the liquid phase. Our model predicts that ONOOH exhibits a net production in the liquid phase, mainly in the first 2 nm depth below the gas–liquid interface and both in the center and towards the edges. The production of ONOOH is mainly driven by the reaction between NO_2 and OH (R39). The reaction between NO and HO_2 (R38) becomes important in the bulk liquid. The main loss of ONOOH is based on reactions with H_2O ((R41) and (R42)). Both processes are important in the interface region and in the bulk liquid. In the interface region (R41) counts for 65% (IF65) of the ONOOH production and (R42) for 30% (IF30), while in the bulk the importance has shifted to 30 and 65%, respectively. Nevertheless, its production is two orders of magnitude faster than its loss during plasma treatment. After plasma treatment, the situation reverses. Indeed, as the production of ONOOH mainly depends on short-lived species, while the loss is due to reaction with H_2O (clearly long-lived species), this explains why ONOOH is lost within 10 seconds after plasma treatment (Fig. 9).

HO_2 is mainly lost in its ionic form (O_2^-) in the liquid phase, just below the gas–liquid interface, upon reaction with OH radicals (R10). The rate of its production (again just below the gas–liquid interface, upon reaction of OH radicals with H_2O_2; (R9)) is a factor of 40 lower than its loss rate. In Fig. 9, we can see that the concentration of HO_2 rapidly increases upon plasma treatment, after which it remains constant in the liquid phase during plasma treatment. This indicates that all the HO_2 that is transported into the liquid from the gas phase immediately reacts away with OH radicals, and no HO_2 can accumulate additionally in the bulk liquid. This also explains why its concentration drops within 10 seconds after plasma treatment. Indeed, once the transport from the gas phase stops, the concentration of HO_2 starts to drop to zero, because all HO_2 that came in from the gas phase reacts away.

For O_3 only one production reaction is included in the model, *i.e.*, recombination between O and O_2 (R16). Other than all the other long-lived species, O_3 has a low Henry's constant, which means it has an equilibrium towards the gas phase. O_3 is net produced in the liquid phase, mainly towards the edges of the well and in the first 2 nm depth below the gas–liquid interface. The most important loss reactions of O_3 are reactions with NO_2^- and HNO ((R37) and (R45)), but the total loss rate of O_3 is three orders of magnitude lower than its production rate. The concentration of O_3 drops relatively slowly after plasma treatment (Fig. 9), because its loss is not due to chemical reactions in the liquid phase, but due to evaporation into the gas phase as a result of its low Henry's constant.

Although ONOOH, HO_2, and O_3 are able to accumulate to some extent in the liquid during plasma treatment, their concentrations clearly drop after plasma treatment. For ONOOH and HO_2 this is due to more important loss than production reactions after treatment, while O_3 evaporates into the gas phase because of its low Henry's constant.

O, OH, NO, NO_2, NO_3. As already discussed, the short-lived species (O, OH, NO, NO_2, and NO_3) immediately react in the interface region to form other (long-lived) species. This way, they cannot reach the bulk liquid and thus do not accumulate in the solution. In Table 4, the main loss processes of these short-lived species are listed. These reaction pathways are also added in Fig. 10 in order to give a complete overview of the liquid chemistry.

For both O and NO_3 only one loss reaction is implemented in the 2D model. O reacts with O_2 to form O_3 (R16) and NO_3 reacts with OH^- to form OH radicals and NO_3^- (R50). OH is lost

Table 4 Main loss processes for the short-lived species (analyzed during plasma treatment) and their contribution to the total loss. Since these species do not reach the bulk liquid, the analysis is done only for the interface. The numbers indicate the % contribution for the loss in the interface. A reaction with a star (*) behind it is the only loss reaction for that species implemented in the 2D model. The reaction numbers correspond to Table S4 (ESI). Reactions between 2 species resulting in 1 species are possible because of the omnipresence of H_2O molecules in the liquid (conservation of momentum and energy)

Species	Main loss reactions	%
O	(16) $O + O_2 \rightarrow O_3$ (*)	
OH	(10) $OH + O_2^- \rightarrow OH^- + O_2$	60
	(24) $OH + NO_2^- \rightarrow OH^- + NO_2$	25
	(6) $OH + OH \rightarrow H_2O_2$	10
NO	(33) $NO + OH \rightarrow HNO_2$	95
NO_2	(34) $NO_2 + OH \rightarrow HNO_3$	50
	(39) $NO_2 + OH \rightarrow ONOOH$	50
NO_3	(50) $NO_3 + OH^- \rightarrow OH + NO_3^-$ (*)	

due to three processes, which are all important for the production or loss of long-lived species. It reacts with O_2^- (R10) and NO_2^- (R24) causing the loss of these species, and it forms H_2O_2 *via* (R6). NO is lost in the most important reaction to form HNO_2 (R33), and for NO_2 the loss results in the formation of HNO_3 (R34) and ONOOH (R39).

Conclusion

We presented the combination of a 0D chemical kinetics model and a 2D axisymmetric fluid dynamics model to investigate the plasma treatment of a buffered water solution with the kINPen® plasma jet, as well as the stability of the generated reactive species after treatment. The 0D model is used to simulate the actual plasma discharge and to provide the gas phase densities at the end of the visible afterglow as input for the 2D model. In addition, it gives information on the most important species and reactions for both the gas and liquid phase, to be introduced in the 2D model. The 2D model simulates the gas and liquid flow dynamics, as well the transport and chemistry of the species in both the gas and the liquid phase. We pay special attention to the production and loss processes for the various species in the liquid phase. By comparing the gas phase densities from the 0D model (already extensively validated with experiments in previous work) with those in the 2D model, we showed that – despite the limited set of species and reactions introduced in the 2D model (in contrast to the 0D model) – the main chemistry is still valid.

In comparison with our previous 2D fluid dynamics model, we can conclude that the gas and liquid flow patterns are highly dependent on the size and shape of the liquid vessel. In the present study, we considered a small well with only 2 mL of liquid. This results in (1) the absence of ambient air in the gas phase between the plasma jet and the liquid surface (resulting in an increasing NO density in the gas phase), and (2) the formation of only one vortex in the liquid near the edge of the well (instead of two reversed vortices in the larger beaker of 135 mL in our previous 2D model).

Only the long-lived species H_2O_2, HNO_2, HNO_3, HO_2, O_3, and ONOOH are able to accumulate into the bulk liquid. The other species are short-lived and only appear in the region a few nm below the gas–liquid interface. After plasma treatment, only the concentrations of H_2O_2, HNO_2, and HNO_3 are constant, while the other long-lived species are lost in reactions (*i.e.* within 10 seconds, for HO_2, and ONOOH) or due to evaporation in the gas phase (for O_3, because of its low Henry's constant). It should be noted that the calculated concentrations of H_2O_2, HNO_2, and HNO_3 are not yet in quantitative agreement with our experimental observations. This can be attributed to the static interface defined in the model. In the future we will try to make the interface more dynamic, in order to reach also quantitative agreement between the model and the experiments. However, the present model already gives important insight in the complex liquid chemistry. By analyzing the main production and loss reactions for the long-lived species, we can explain why only H_2O_2, HNO_2, and HNO_3 are stable in the liquid (*i.e.* all their production and loss processes in the liquid only depend on reactions with short-lived species), while O_3, HO_2, and ONOOH are not.

We believe that this study provides valuable insight into the plasma–liquid interaction of a plasma jet with a buffered water solution, as well as into the liquid chemistry during and after plasma treatment. This information is very useful for the application of plasma-treated liquids in biomedicine, both for the generation of PTLs and for the stability of reactive species during storage of PTLs.

Conflicts of interest

There are no conflicts to declare.

Acknowledgements

We acknowledge financial support from the Fund for Scientific Research (FWO) Flanders (Grant No. 1161919N). The authors would like to thank Jonas Van der Paal and Yury Gorbanev (UAntwerp, PLASMANT group) for the valuable discussions about the 0D model and plasma–liquid interactions.

References

1 A. Kramer, J. Lademann, C. Bender, A. Sckell, B. Hartmann, S. Münch, P. Hinz, A. Ekkernkamp, R. Matthes, I. Koban, I. Partecke, C. D. Heidecke, K. Masur, S. Reuter, K. D. Weltmann, S. Koch and O. Assadian, *Clin. Plasma Med.*, 2013, **1**, 11–18.
2 S. Emmert, F. Brehmer, H. Holger, A. Helmke, N. Mertens, R. Ahmed, D. Simon, D. Wandke, W. Maus-friedrichs, W. Vi, M. P. Sch and D. Georg, *Clin. Plasma Med.*, 2013, **1**, 24–29.
3 G. Isbary, G. Morfill, H. U. Schmidt, M. Georgi, K. Ramrath, J. Heinlin, S. Karrer, M. Landthaler, T. Shimizu, B. Steffes, W. Bunk, R. Monetti, J. L. Zimmermann, R. Pompl and W. Stolz, *Br. J. Dermatol.*, 2010, **163**, 78–82.
4 G. Fridman, M. Peddinghaus, M. Balasubramanian, H. Ayan, A. Fridman, A. Gutsol and A. Brooks, *Plasma Chem. Plasma Process.*, 2006, **26**, 425–442.
5 J. Schlegel, J. Köritzer and V. Boxhammer, *Clin. Plasma Med.*, 2013, **1**, 2–7.
6 M. Ishaq, M. M. Evans and K. K. Ostrikov, *Int. J. Cancer*, 2014, **134**, 1517–1528.
7 X. Lu, G. V. Naidis, M. Laroussi, S. Reuter, D. B. Graves and K. Ostrikov, *Phys. Rep.*, 2016, **630**, 1–84.
8 T. Sato, M. Yokoyama and K. Johkura, *J. Phys. D: Appl. Phys.*, 2011, **44**, 372001.
9 M. Vandamme, E. Robert, S. Lerondel, V. Sarron, D. Ries, S. Dozias, J. Sobilo, D. Gosset, C. Kieda, B. Legrain, J. M. Pouvesle and A. L. Pape, *Int. J. Cancer*, 2012, **130**, 2185–2194.
10 T. Adachi, H. Tanaka, S. Nonomura, H. Hara, S. I. Kondo and M. Hori, *Free Radical Biol. Med.*, 2015, **79**, 28–44.
11 C. Klinkhammer, C. Verlackt, F. Kogelheide, A. Bogaerts, N. Metzler-nolte, K. Stapelmann, M. Havenith and J. Lackmann, *Sci. Rep.*, 2017, **7**, 13828.

12 N. Kumar, P. Attri and S. Dewilde, *J. Phys. D: Appl. Phys.*, 2018, **51**, 255401.
13 H. Tanaka, M. Mizuno, K. Ishikawa, K. Nakamura, H. Kajiyama, H. Kano, F. Kikkawa and M. Hori, *Plasma Med.*, 2011, **1**, 265–277.
14 D. Yan, J. H. Sherman, X. Cheng, E. Ratovitski, J. Canady and M. Keidar, *Appl. Phys. Lett.*, 2014, **105**, 224101.
15 S. Vermeylen, J. De Waele, S. Vanuytsel, J. De Backer, J. Van der Paal, M. Ramakers, K. Leyssens, E. Marcq, J. Van Audenaerde, E. L. J. Smits, S. Dewilde and A. Bogaerts, *Plasma Processes Polym.*, 2016, **13**, 1195–1205.
16 D. Yan, N. Nourmohammadi, K. Bian, F. Murad, J. H. Sherman and M. Keidar, *Sci. Rep.*, 2016, **6**, 26016.
17 W. Van Boxem, J. Van Der Paal, Y. Gorbanev, S. Vanuytsel, E. Smits, S. Dewilde and A. Bogaerts, *Sci. Rep.*, 2017, **7**, 16478.
18 A. Privat-Maldonado, Y. Gorbanev, S. Dewilde, E. Smits and A. Bogaerts, *Cancers*, 2018, **10**, 394.
19 H. Tanaka, K. Nakamura, M. Mizuno, K. Ishikawa and K. Takeda, *Sci. Rep.*, 2016, **6**, 36282.
20 S. Mohades, M. Laroussi and V. Maruthamuthu, *J. Phys. D: Appl. Phys.*, 2017, **50**, 185205.
21 S. Takeda, S. Yamada, N. Hattori, K. Nakamura, H. Tanaka, H. Kajiyama, M. Kanda, D. Kobayashi, C. Tanaka, T. Fujii, M. Fujiwara, M. Mizuno, M. Hori and Y. Kodera, *Ann. Surg. Oncol.*, 2017, **24**, 1188–1194.
22 P. J. Bruggeman, M. J. Kushner, B. R. Locke, J. G. E. Gardeniers, W. G. Graham, D. B. Graves, R. C. H. M. Hofman-Caris, D. Maric, J. P. Reid, E. Ceriani, D. Fernandez Rivas, J. E. Foster, S. C. Garrick, Y. Gorbanev, S. Hamaguchi, F. Iza, H. Jablonowski, E. Klimova, J. Kolb, F. Krcma, P. Lukes, Z. Machala, I. Marinov, D. Mariotti, S. Mededovic Thagard, D. Minakata, E. C. Neyts, J. Pawlat, Z. L. Petrovic, R. Pflieger, S. Reuter, D. C. Schram, S. Schröter, M. Shiraiwa, B. Tarabová, P. A. Tsai, J. R. R. Verlet, T. von Woedtke, K. R. Wilson, K. Yasui and G. Zvereva, *Plasma Sources Sci. Technol.*, 2016, **25**, 053002.
23 N. Y. Babaeva, W. Tian and M. J. Kushner, *J. Phys. D: Appl. Phys.*, 2014, **47**, 1–11.
24 C. Chen, D. X. Liu, Z. C. Liu, A. J. Yang, H. L. Chen, G. Shama and M. G. Kong, *Plasma Chem. Plasma Process.*, 2014, **34**, 403–441.
25 A. M. Lietz and M. J. Kushner, *J. Phys. D: Appl. Phys.*, 2016, **49**, 425204.
26 D. X. Liu, Z. C. Liu, C. Chen, A. J. Yang, D. Li, M. Z. Rong, H. L. Chen and M. G. Kong, *Sci. Rep.*, 2016, **6**, 23737.
27 W. Tian and M. J. Kushner, *J. Phys. D: Appl. Phys.*, 2014, **47**, 165201.
28 Y. Gorbanev, C. C. W. Verlackt, S. Tinck, E. Tuenter, K. Foubert, P. Cos and A. Bogaerts, *Phys. Chem. Chem. Phys.*, 2018, **20**, 2797–2808.
29 W. Van Gaens and A. Bogaerts, *J. Phys. D: Appl. Phys.*, 2013, **46**, 275201.
30 K. Wende, P. Williams, J. Dalluge, W. Van Gaens, H. Aboubakr, J. Bischof, T. von Woedtke, S. M. Goyal, K.-D. Weltmann, A. Bogaerts, K. Masur and P. J. Bruggeman, *Biointerphases*, 2015, **10**, 029518.
31 W. Van Gaens, P. J. Bruggeman and A. Bogaerts, *New J. Phys.*, 2014, **16**, 063054.
32 J. Du, Z. Liu, C. Bai, L. Li, Y. Zhao, L. Wang and J. Pan, *Eur. Phys. J. D*, 2018, **72**, 179.
33 A. Lindsay, C. Anderson, E. Slikboer, S. Shannon and D. Graves, *J. Phys. D: Appl. Phys.*, 2015, **48**, 424007.
34 A. M. Lietz and M. J. Kushner, *J. Appl. Phys.*, 2018, **124**, 153303.
35 S. A. Norberg, G. M. Parsey, A. M. Lietz, E. Johnsen and M. J. Kushner, *J. Phys.*, 2019, **52**, 015201.
36 C. C. W. Verlackt, W. Van Boxem and A. Bogaerts, *Phys. Chem. Chem. Phys.*, 2018, **20**, 6845–6859.
37 L. C. P. S. Pancheshnyi, B. Eismann and G. J. M. Hagelaar, ZDPlasKin, Univ. Toulouse, LAPLACE, CNRS-UPS-INP, Toulouse, Fr, 2008.
38 W. Van Gaens and A. Bogaerts, *Plasma Sources Sci. Technol.*, 2014, **23**, 035015.
39 K. T. Trinh, 2010, arXiv:1007.0810.
40 D. C. Wilcox, *Turbulence Modelling for CFD*, DCW Industries, Inc., 1993.
41 A. Schmidt-Bleker, J. Winter, A. Bösel, S. Reuter and K.-D. Weltmann, *Plasma Sources Sci. Technol.*, 2016, **25**, 015005.
42 G. Eisenberg, *Ind. Eng. Chem., Anal. Ed.*, 1943, **15**, 327–328.
43 J. F. M. Van Rens, J. T. Schoof, F. C. Ummelen, D. C. Van Vugt, P. J. Bruggeman and E. M. Van Veldhuizen, *IEEE Trans. Plasma Sci.*, 2014, **42**, 2622–2623.
44 W. Van Gaens, S. Iseni, A. Schmidt-Bleker, K. D. Weltmann, S. Reuter and A. Bogaerts, *New J. Phys.*, 2015, **17**, 033003.
45 L. Hansen, A. Schmidt-Bleker, R. Bansemer, H. Kersten, K.-D. Weltmann and S. Reuter, *J. Phys. D: Appl. Phys.*, 2018, **51**, 474002.
46 J. Winter, H. Tresp, M. U. Hammer, S. Iseni, S. Kupsch, A. Schmidt-Bleker, K. Wende, M. Dünnbier, K. Masur, K.-D. Weltmann and S. Reuter, *J. Phys. D: Appl. Phys.*, 2014, **47**, 285401.
47 P. Lukes, E. Dolezalova, I. Sisrova and M. Clupek, *Plasma Sources Sci. Technol.*, 2014, **23**, 015019.
48 V. V. Kovačević, B. P. Dojčinović, M. Jović, G. M. Roglić, B. M. Obradović and M. M. Kuraica, *J. Phys. D: Appl. Phys.*, 2017, **50**, 155205.
49 F. Girard, V. Badets, S. Blanc, K. Gazeli, L. Marlin, L. Authier, P. Svarnas, N. Sojic, F. Clément and S. Arbault, *RSC Adv.*, 2016, **6**, 78457–78467.

